IEEE Access
Multidisciplinary | Rapid Review | Open Access Journal

Received March 24, 2021, accepted April 2, 2021, date of publication April 7, 2021, date of current version April 14, 2021.

Digital Object Identifier 10.1109/ACCESS.2021.3071554

High-Accuracy Position-Aware Robot for Agricultural Automation Using Low-Cost IMU-Coupled Triple-Laser-Guided (TLG) System

SUPOD KAEWKORN[1], MONGKOL EKPANYAPONG[1], AND UKRIT THAMMA[2]
[1]School of Engineering and Technology, Asian Institute of Technology, Khlong Nueng 12120, Thailand
[2]College of Industrial Technology, King Mongkut's University of Technology North Bangkok, Bangkok 10800, Thailand

Corresponding author: Ukrit Thamma (ukritthamma@gmail.com)

ABSTRACT A novel, low-cost approach to high-accuracy robot localization for agricultural applications using an image-processing triple-laser-guided (TLG) system coupled with an inertial measurement unit (IMU) is presented in this paper. The TLG system consists of a laser-pointing unit (LPU) at the base station and a laser-target unit (LTU) at the mobile robot. The robot's XYZ position and heading are determined from the positions and the angles relative to the field of both LPU and LTU. The robot's roll and pitch are determined by the IMU sensor fusion with complementary filter. The IMU-coupled TLG system is demonstrated on an outdoor, 20 × 21 m flat field at various light intensities. The overall lateral and vertical accuracies of the IMU-coupled TLG system are 1.68 cm and 0.59 cm, respectively. The overall heading, roll, and pitch accuracies of the IMU-coupled TLG system are 0.90°, 0.78°, and 0.76°, respectively. The lateral and heading accuracies of the IMU-coupled TLG system are found to be comparable to commercially available GNSS-INS systems from NovAtel and Trimble, while the total cost of the IMU-coupled TLG system is only a fraction of the total cost of the commercially available localization systems.

INDEX TERMS Laser tracking system, localization, inertial measurement unit (IMU), sensor fusion, position control.

I. INTRODUCTION

Automatic machinery has been widely researched and applied in the agricultural industry to increase productivity and reduce costs. Specifically, automatic guided robots are of interest for many agricultural tasks, i.e., seeding, weed controlling, soil tilling, fertilizing, watering, and harvesting. To effectively perform these complex open-field tasks, accurate and precise localization of these agricultural robots, including XYZ position, heading, and attitude (roll and pitch tilts), are essential. Several principles of localization sensors for agricultural robots are real-time kinematic global navigation satellite systems (RTK GNSS)[1]–[5], landmarks detection [6], light laser detection and ranging (LiDAR) [7]–[8], radar [9], sensor fusion with camera [10]–[13], ultrasonic [14], multi-sensor fusion [15], [16], beacons based [17], localization and mapping (SLAM) [18], laser range finder (LRF) [19], and inertial measurement unit (IMU) [20]. Particularly, RTK GNSS coupled with inertial navigation systems (INS) is extensively employed by farmers due to its relatively higher accuracy and precision compared to other sensing techniques. In the RTK GNSS-INS system, the robot's position is determined based on the trilateration of the Universal Transverse Mercator obtained through a constellation of satellites, while the robot's angles of orientation are obtained by real-time measurements of angular velocity, linear acceleration, and the earth's magnetic field via the INS.

Nonetheless, there are a few drawbacks to the agricultural practicality of the RTK GNSS-INS system. First, the RTK GNSS-INS system's accuracy and precision depend on the transmissivity of satellites' signals. The decrease in the satellite transmissivity due to signal blockage and multipath effect from neighboring buildings or trees and cloudy weather can lead to the deterioration of the RTK GNSS-INS system's positioning accuracy and precision. Hence, this limits the operation of RTK GNSS-INS system to only an open, outdoor environment under open-sky conditions. Second, the heading determination in the RTK GNSS-INS system partly relies on the sensor fusion between the earth's magnetic field

The associate editor coordinating the review of this manuscript and approving it for publication was Yang Tang.

measurement from magnetometers and the angular velocity measurement from gyroscopes with tilt compensation accelerometers in the INS unit. Due to geographical variation in the earth's magnetic field, the RTK GNSS-INS system requires a time-consuming calibration when the operating field has been moved. Moreover, the measurement of the earth's magnetic field can easily be interfered with by the surrounding environment, such as metallic structures and electronic equipment; therefore, the INS's heading measurement can, at times, be inconsistent and unreliable.

In recent years, there are advancements in GNSS-based localization systems for agriculture to tackle the previously mentioned drawbacks. For example, integration of RTK GNSS-based system with LiDAR [21] and Untethered Dead Reckoning (UDR) [22] have been shown to improve the accuracy and precision while operating in GNSS-denied areas. In some applications, multi-antenna GNSS systems were shown to improve the heading accuracy and RTK availability/success rate in signal-challenging areas [23]–[25]. However, all of these could lead to increase cost and complexity to the end users significantly.

Lastly, the RTK GNSS-INS system is currently costly and not affordable to small-scale farming operations. To provide an alternative to the conventional, expensive RTK GNSS-INS system, this paper presents a low-cost, inertial measurement unit (IMU)-coupled triple-laser-guided (TLG) system that provides high localization accuracy and precision for both indoor and outdoor environment at a substantially lower cost.

II. BRIEF INNOVATION DESCRIPTION

The IMU-coupled TLG system consists of a base station with a laser-pointing unit (LPU) and a mobile unit with a laser-target unit (LTU). The LPU consists of two laser pointers and a laser rangefinder module. The LTU consists of three laser targets: two projection targets to detect the projected laser pointers and one target to reflect the laser rangefinder from the LPU. The high accuracy and precision of localization are achieved by the innovative design of interaction between the LPU and LTU which is briefly described as follows:

- The LPU is controlled to point at the middle of the LTU while the LTU is controlled so that the laser targets are perpendicular to the laser-pointing beams.
- The interactive controlling of the LPU and LTU is achieved by analyzing the projected positions of the LPU's laser pointers on the LTU's projection targets via image processing.
- With the LPU pointing perpendicularly at the center of the LTU, the position and heading of the mobile unit relative to the laser base station can be accurately and precisely determined using the distance measured by the laser rangefinder, the fanning angle of LPU, and the relative heading angle of the LTU.

III. EQUIPMENT DESCRIPTION

The IMU-coupled TLG system demonstrated in this study consists of a laser base station and a mobile unit, as shown in Fig. 1. Computer software is used for data recording, manual control, and PID setup for both the base station and the mobile unit.

A. LASER BASE STATION

The laser base station comprises a base frame, a laser-pointing unit (LPU), and a fanning-vertical control unit (FVCU), as shown in Fig. 2. The base frame is constructed as a rectangular box frame with dimensions of 30 cm in width, 50 cm in length, and 110 cm in height, using hollow steel bars. Four level-adjusting poles are applied as the base frame's legs.

The LPU is designed to track the position and control the heading of the mobile unit. The LPU holds three lasers: a heading-measuring laser (HML), a position-measuring laser (PML), and a distance-measuring laser (DML). The HML, the PML, and the DML are at the top, in the middle, and at the bottom position of the LPU, respectively, with a 12-cm vertical separation. The lasers are situated to point in the same direction and parallel to the ground. A 405-nm violet laser pointer, a 650-nm red laser pointer, and a 650-nm red laser rangefinder are applied as the HML, the PML, and the DML, respectively.

The FVCU, devised to track and control the linear and fanning motions of the LPU, consists of a rotary actuator and a linear actuator (Fig. 2). The rotary actuator employs a micro-stepping motor and an incremental encoder with a maximum angle of rotation of 180° and a rotating resolution of 9.38 × 10.3 °/step. The linear actuator is driven by a DC motor and controls its moving arm position using an incremental encoder and PID position control with the maximum moving distance of 30 cm. In the FVCU, the rotatory actuator is attached to the moving arm of the linear actuator. It is oriented so that its plane of rotation is perpendicular to the linear actuator's uniaxial motion.

To allow vertical control along the Z-axis and fanning control in the XY-plane of the LPU, the LPU is attached to the rotary actuator of the FVCU, and then the LPU-FVCU assembly is secured on the base frame so that the linear actuator of the FVCU is in the vertical position. A microcontroller unit (MCU) is employed to process the data from the FVCU and the LPU, to control the actuators in the FVCU, and to remotely communicate the data via 433-MHz radio frequency (RF).

B. MOBILE UNIT

The mobile unit consists of a skid-steering robot, a laser-target unit (LTU), a heading control unit (HCU), and an attitude-measuring unit (AMU), as illustrated in Fig. 3. The skid-steering robot is a four-wheel-drive using four 24-volt DC motors with H-bridge PWM drivers controlled by an MCU. The skid-steering robot's commands from an external host are remotely transmitted to the MCU via 433-MHz RF. The robot's frame dimensions are 50 cm in width, 70 cm in length, and 140 cm in height, and the size

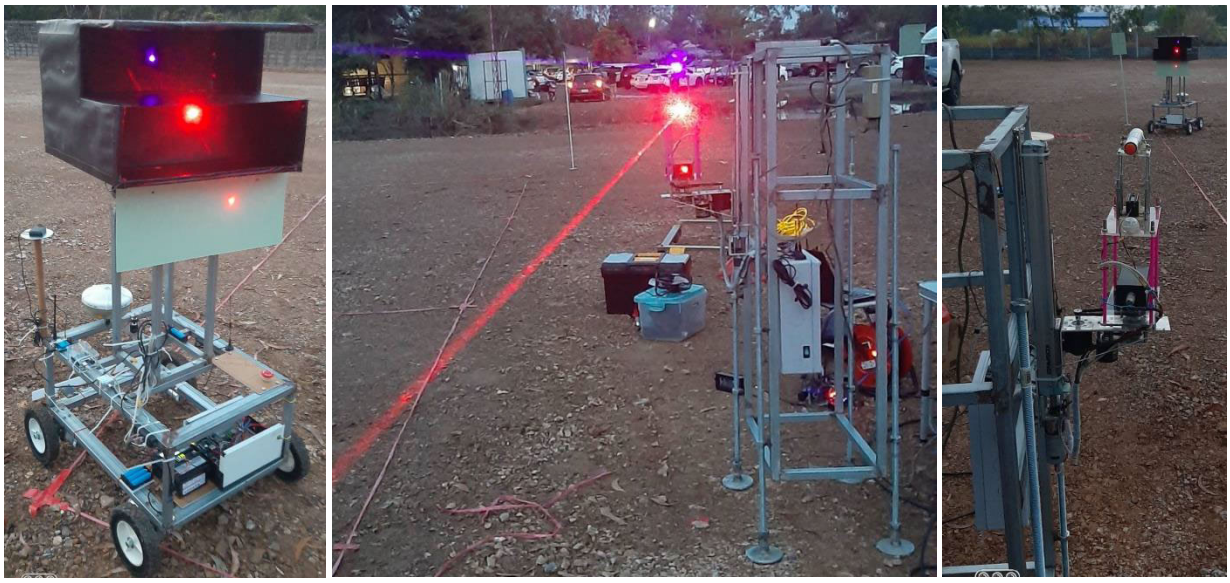

FIGURE 1. IMU-coupled TLG system.

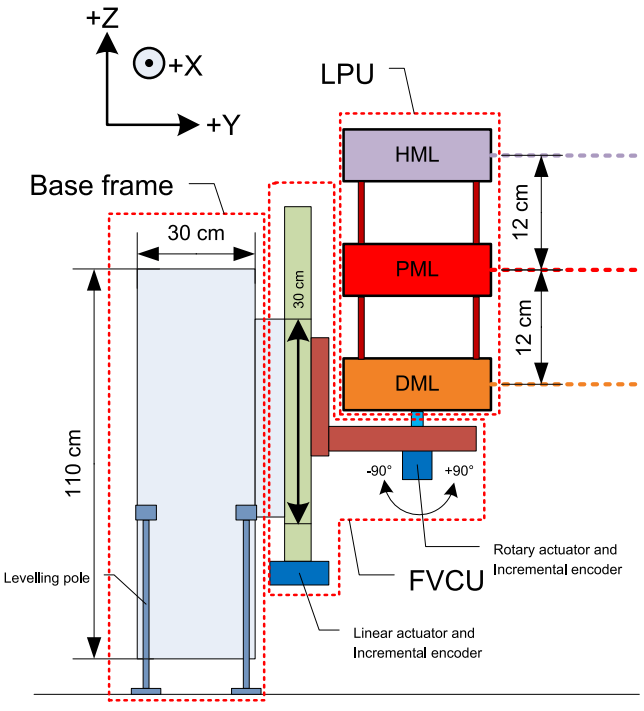

FIGURE 2. Schematic illustration of the laser base station.

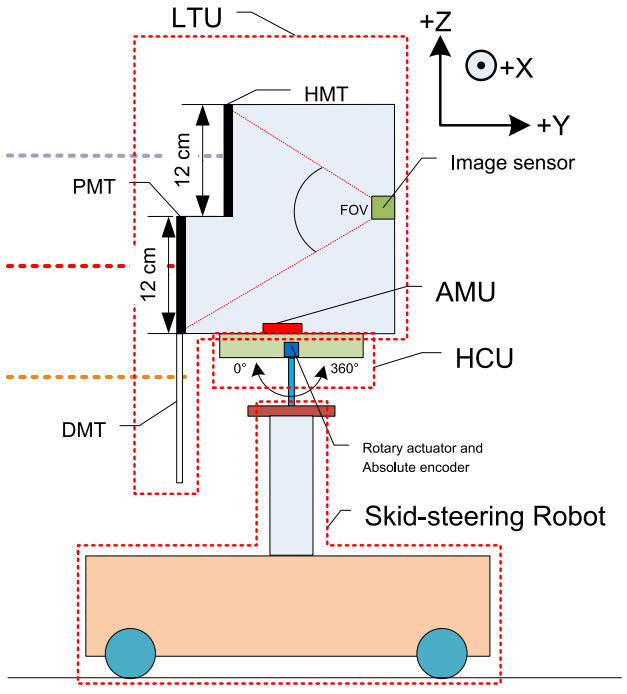

FIGURE 3. Schematic illustration of the mobile unit.

of the wheels is 20.4 cm in diameter. The robot's maximum speed is set at 1.5 m/s.

The LTU includes a heading-measuring target (HMT), a position-measuring target (PMT), a distance-measuring target (DMT), and an image sensor. The HMT and the PMT, assigned to project the HML and the PML for heading control and measurement, are 12 cm × 50 cm projector screens made from black, translucent paper. The DMT, assigned to reflect the DML for distance measurement, is a 12 cm × 50 cm laser reflecting screen made from a white, opaque plastic sheet. The HMT, the PMT, and the DMT are placed at the top, in the middle, and at the bottom position of the LTU, respectively, with a 12-cm vertical separation between their centers. The image sensor used to detect and determine the positions of the projected HML and PML on the HMT's and PMT's screens is a Pixy2 CMUcam5 smart camera with a frame rate of 60 frames per second and

TABLE 1. Cost breakdown of the IMU-coupled TLG system (based on retail and online prices plus shipping for Bangkok, Thailand in February 2021).

Hardware Group	Subgroup	Component Descriptions	Cost in USD
Laser Base Station	Base Frame	Materials and fabrication	$150.00
	Laser-pointing Unit (LPU)	50-meter laser rangefinder module – 1 unit	$90.00
		405-nm violet laser pointer – 1 unit	$20.00
		605-nm red laser pointer – 1 unit	$10.00
	Fanning-vertical Control Unit (FVCU)	OMRON E6B2-CWZ6C rotary encoder– 2 units	$70.00
		DRV8825 stepper motor driver – 1 unit	$10.00
		Rtelligent Nema 17 stepper motor – 1 unit	$20.00
		Linear Actuator – 1 unit	$70.00
		STM32F3 Discovery microcontroller – 1 unit	$20.00
		Circuit components	$50.00
Mobile Unit	Laser-target Unit (LTU)	Structural frame – materials and fabrication	$100.00
		Pixy 2 CMUcam5 image sensor – 1 unit	$150.00
	Heading Control Unit (HCU)	DC-geared motor – 1 unit	$15.00
		L298N H-Bridge DC-motor driver – 1 unit	$10.00
		5V 1024-pulse absolute encoder– 1 unit	$50.00
		Circuit components	$50.00
		Battery – 1 unit	$25.00
	Attitude-measuring Unit (AMU)	IMU with STM32F3 Discovery microcontroller	$20.00
Wireless Communication	Wireless Transceivers	433-MHz radio frequency (RF) modules – 8 units	$20.00
Estimated Total			$950.00

the field of view (FOV) covering both HMT and PMT. The HMT, the PMT, and the image sensor are placed in a dark enclosure, where the HMT and the PMT are placed in front of the image sensor at 18 cm and 30 cm away, respectively.

The positions of the projected HML on the HMT and the projected PML on the PMT are used to control the LPU and LTU so that the lasers perpendicularly pointing at the center of their assigned targets. This is critical for the IMU-coupled TLG system to achieve the highest accuracy and precision in localization and is elaborated in further detail in Control Description. The Pixy2 smart camera is programmed to find a violet laser blob from the HML on the HMT and a red laser blob from the PML on the PMT. The centroids of the area of these laser blobs are then quantified via image processing of the Pixy2 smart camera and reported to the microcontroller as the positions of the projected lasers. To avoid interference for the image sensor's detection of projected HML and PML, the maximum light intensity allowed on the HMT and the PMT is 20,000 lux.

The HCU is a 360° bidirectional, rotatable stand. A DC-motor rotary actuator with PID position control drives and controls its rotational motion and an absolute encoder measures its angle of rotation. For attitude (roll and pitch tilts) measurement, the AMU utilizes a low-cost 6DoF IMU where roll and pitch are computed using IMU sensor fusion with complementary filter [26], [27].

For the complete assembly of the mobile unit, the HCU is secured on top and at the center of the robot's frame. The LTU and AMU are then placed and centered on the HCU, allowing 360° rotation of the LTU and the AMU on the mobile unit. An MCU is utilized to process the data from the LTU, the HCU, and the AMU, control the rotary actuator in the HCU, and remotely communicate the data via 433-MHz RF.

IV. SYSTEM COST BREAKDOWN

The IMU-coupled TLG system's total cost mainly comes from the structural, mechanical, electronic components of three hardware groups: the laser base station, the mobile unit, and the wireless communication components. The cost breakdown was based on retail and online prices plus shipping for Bangkok, Thailand, in February 2021 and is summarized in Table 1. The total cost of the IMU-coupled TLG system for this study was $950 in USD. It is to be noted that the skid-steering robot's cost is not included since its purpose in this study was only to be a model rover for demonstrating the performance of the IMU-coupled TLG system.

V. WORKING FIELD AND REFERENCE AXES

An operational area for the mobile unit is a 20 m × 21 m rectangular plain with its reference axes, designated as X, Y, and Z, defined with respect to the laser base station, as depicted in Fig. 4. The origin (0,0,0) of the working field is assigned as the LPU's position at the laser base station. Due to the DML's low measurement accuracy at a close distance to the target, the working field excludes a semicircular area with a radius of 1 m around the laser base station.

VI. INPUT PARAMETERS

The input parameters for determining the robot's position and orientation (attitude and heading) in the IMU-couple TLG system, assuming that both the LPU and LTU are correctly and promptly controlled as elaborated in Control Descriptions, are described as follows:

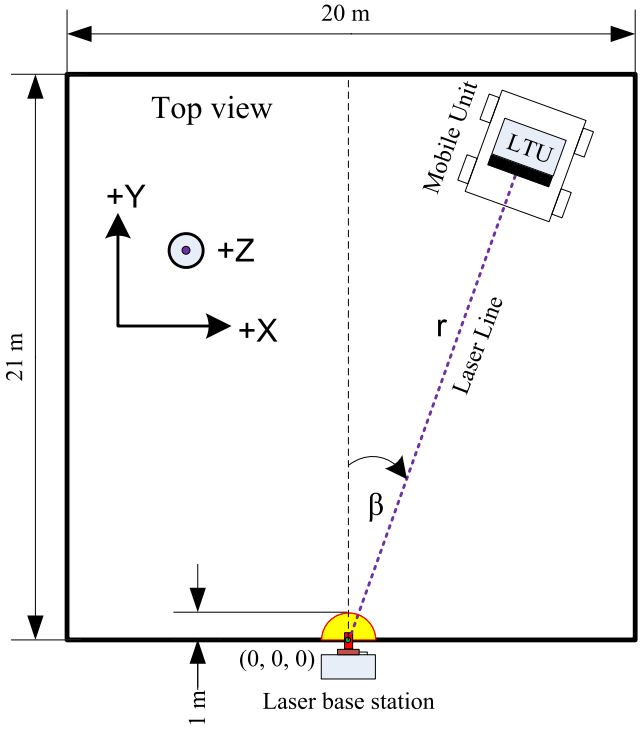

FIGURE 4. Working field and reference axes.

1) The distance between the LPU and the LTU (r) measured by the DML on the LPU at the laser base station (see Fig. 4)
2) The fanning angle of the LPU (β) measured by the FVCU at the laser base station (see Fig. 4)
3) The height of the LPU (h) measured by the FVCU at the laser base station
4) The roll tilt of the LTU (θ) measured by the AMU on the mobile unit
5) The pitch tilt of the LTU (ϕ) measured by the AMU on the mobile unit
6) The relative heading angle between the LTU and the skid-steering robot (γ) measured by the HCU on the mobile unit
7) The robot's heading on the field (α) is the sum of β and γ

VII. CONTROL DESCRIPTION

In the IMU-coupled TLG system, the robot's position and heading are computed using the distance between the LPU and LTU and the height and fanning angle of the LPU, which is further elaborated in Determination of Robot's Position and Orientation. For the highest accuracy of distance and heading measurements, the lasers, namely the HML, the PML, and the DML, must be parallel to the ground and perpendicularly pointing at the center of their assigned targets, the HMT, the PMT, and the DMT, respectively. Hence, the LPU on the laser base station and the LTU on the mobile unit must be simultaneously controlled as follows:

A. FANNING ANGLE AND HEIGHT CONTROL OF THE LPU

The LPU control, carried out by the FVCU, aims to keep its lasers' projection at the center of their assigned targets. Since the HML, the PML, and the DML are all on the same LPU's rigid body and positioned with the same vertical separation as the centers of their assigned targets on the LTU, the LPU control is solely focused on maintaining the projected PML position at the center of the PMT. If the PML points perpendicularly to but away from the center of the PMT, it yields center-deviated distances of the projected PML in both X- and Z-axes of the PMT, designated as Err_X^{PMT} and Err_Z^{PMT}, respectively, as illustrated in Fig. 5(a). To keep the projected PML at the PMT's center, the rotary actuator in the FVCU controls the fanning angle (β) of the LPU to minimize the Err_X^{PMT} to zero, while the linear actuator in the FVCU controls the height (h) of the LPU to minimize the Err_Z^{PMT} to zero, as depicted in Fig. 5(b). The LPU fanning angle and height control for Err_X^{PMT} and Err_Z^{PMT} minimization is achieved using a PID control with PWM signaling to the FVCU, as illustrated in Fig. 5(c).

B. HEADING CONTROL OF THE LTU

The aim of the LTU's heading control carried out by the HCU is to ensure that three lasers' beams from the LPU are perpendicular to the targets of the LTU. Suppose the LPU's laser beams are non-perpendicular to the LTU's targets' screens. In that case, there is a difference in the center-deviated distances along the X-axis of the targets between the projected HML on the HMT (Err_X^{HMT}) and the projected PML on the PMT (Err_X^{PMT}), as shown in Fig. 6(a). The magnitude of the difference between Err_X^{HMT} and Err_X^{PMT}, designated as ΔErr_X, is defined as follows:

$$\Delta Err_x = \left| Err_X^{HMT} - Err_X^{PMT} \right| \tag{1}$$

If $\Delta Err_X > 0$, the rotary actuator in HCU rotates the heading of LTU to minimize ΔErr_X to zero, confirming the laser beams' perpendicularity from the LPU to the LTU's targets, as illustrated in Fig. 6(b). The LTU heading control for ΔErr_X minimization is achieved using a PID control with PWM signaling to the HCU, as illustrated in Fig. 6(c).

VIII. DETERMINATION OF ROBOT'S POSITION AND ORIENTATION

Assuming the perpendicularity and centering of the lasers' projections on the targets as described in Control Description, the robot's position and heading in Fig. 7 can be accurately determined as follows:

$$X = r \sin \beta \tag{2}$$

$$Y = r \cos \beta \tag{3}$$

$$Z = h \tag{4}$$

$$Heading(\alpha) = \beta + \gamma \tag{5}$$

The robot's roll (θ) and pitch (ϕ) tilts are calculated via sensor fusion of low-frequency signals from a triple-axis

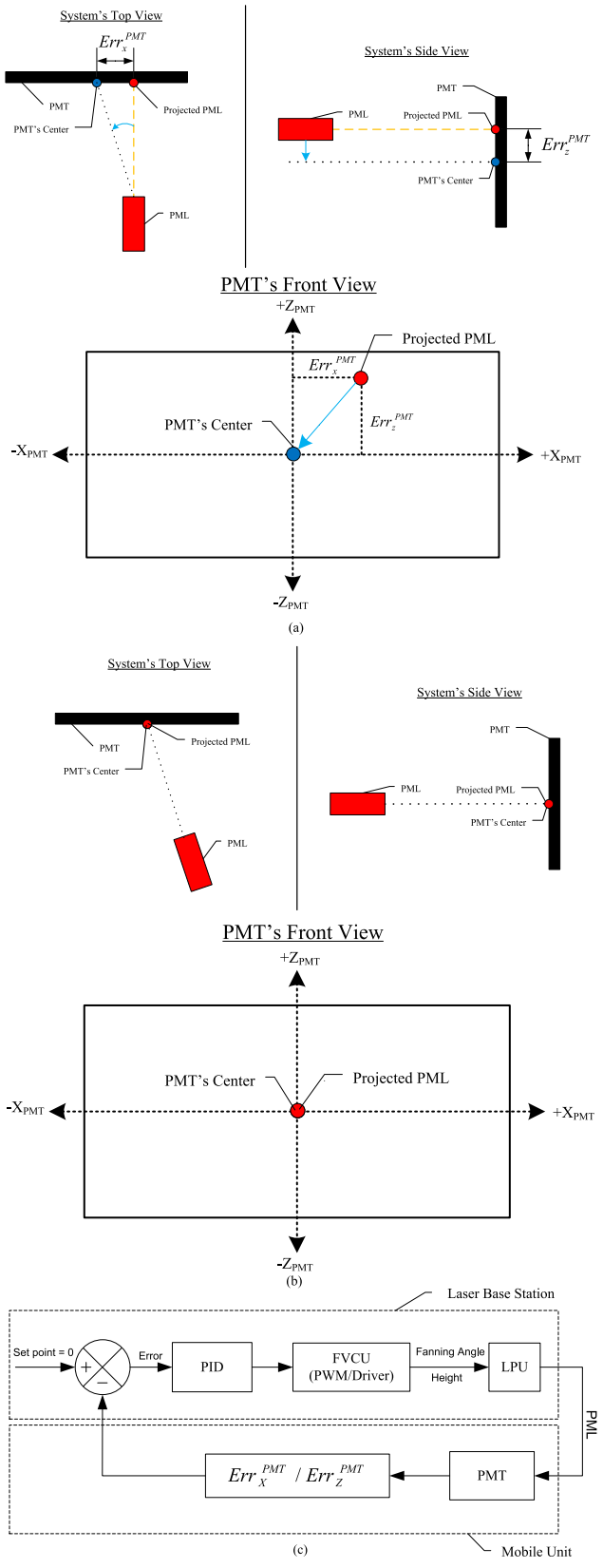

FIGURE 5. LPU control maintaining the projected PML at the center of the PMT: (a) Before LPU control, center-deviated PML projection on the PMT (b) After LPU control, PML projection at the PMT's center (c) LPU fanning angle and height control strategy.

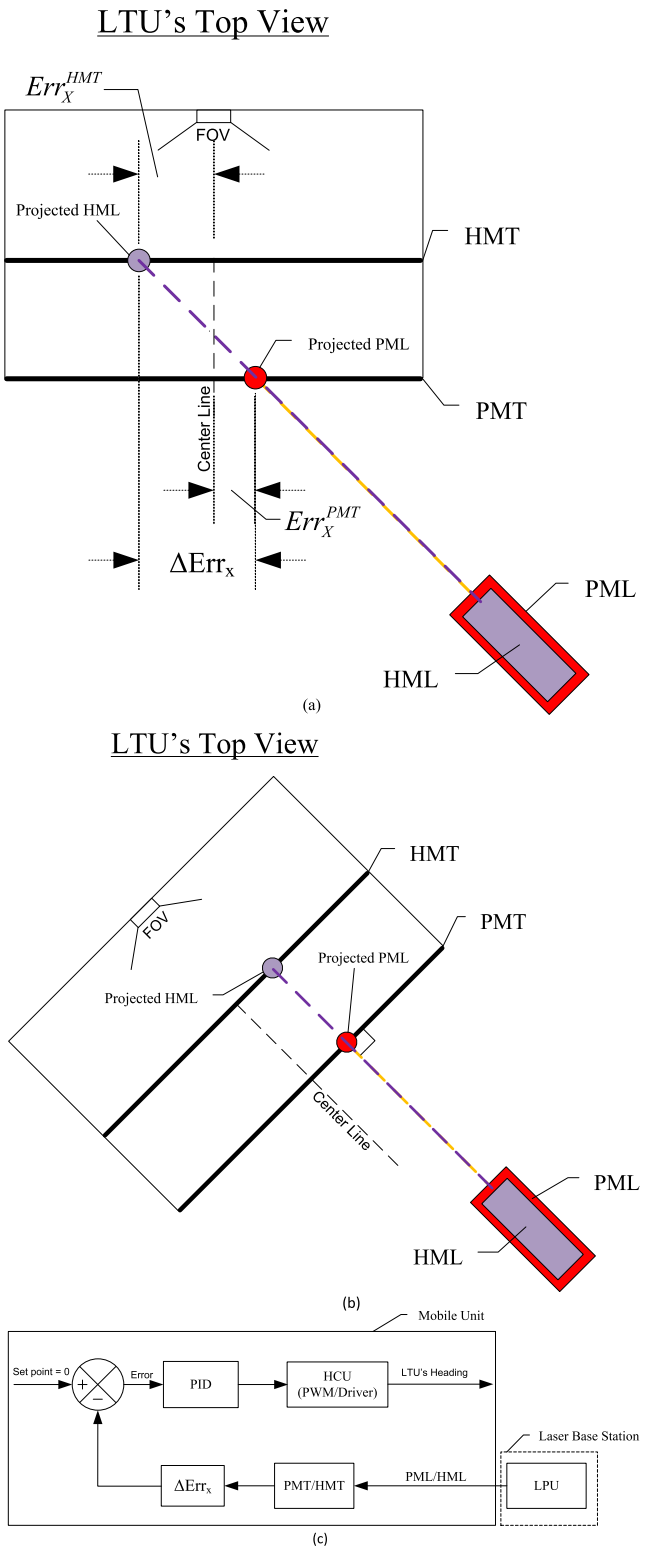

FIGURE 6. LTU control maintaining the perpendicularity of the lasers' beams from the LPU to the LTU's targets: (a) Before LTU control, non-perpendicular lasers' beams to targets (b) After LTU control, perpendicular lasers' beams to targets (c) LTU heading control strategy.

accelerometer and high-frequency signals from a triple-axis gyroscope of a low-cost 6DoF IMU in the AMU through complementary filter [26], [27].

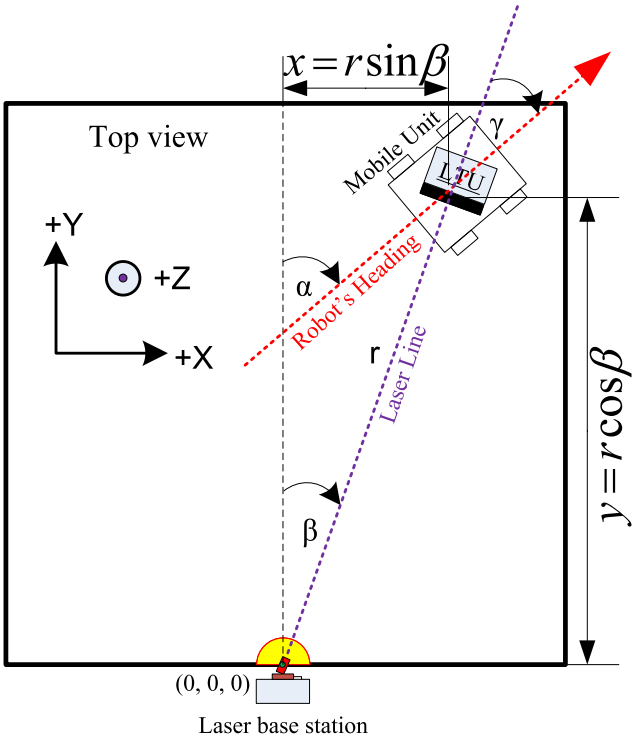

FIGURE 7. Schematic drawing of the IMU-coupled TLG system for the determination of the robot's position and heading.

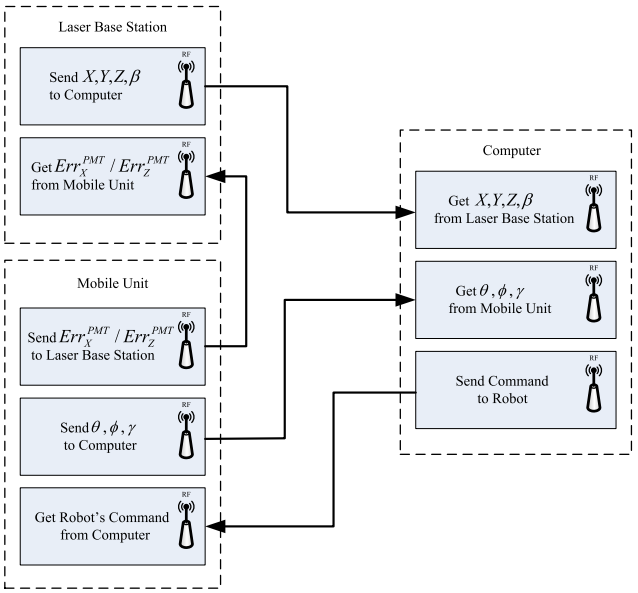

FIGURE 8. Data flow and communication diagram.

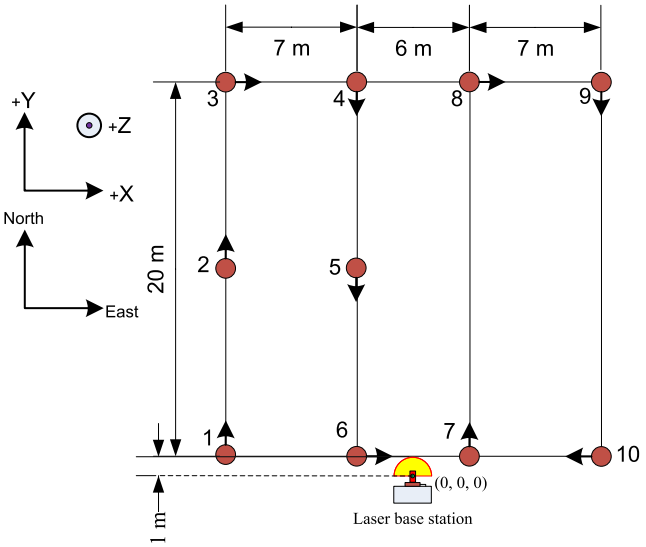

FIGURE 9. Field and designed path for the system demonstration and for the determination of position/orientation accuracy and precision.

IX. DATA FLOW AND COMMUNICATION DIAGRAM

In the IMU-coupled TLG system, the laser base station, the mobile unit, and the computer communicate data among themselves with a sampling rate of 100 ms, as depicted in Fig. 8. The communication is carried out using HC-11 wireless transceiver modules with a frequency band of 433 MHz. For all transceiver modules, the RF power is set to 10 dBm with the data baud rate of 115,200 bps and the transmission delay time of 10 ms. The operating distance of these communication modules is approximately 30 m.

X. METHOD FOR SYSTEM DEMONSTRATION

The operation of a high-accuracy, position-aware robot using the IMU-coupled TLG system was demonstrated in an outdoor setting on a 20 m × 21 m treeless, flat field, as depicted in Fig. 4. The robot was manually controlled to move along a predetermined path on the field from the numbered location 1 to 10, as shown in Fig. 9, without exceeding the maximum speed of 1.2 m/s. The robot's heading was preassigned at the numbered locations with a designated arrow. At each numbered location, the robot was stopped to physically verify its actual position (XYZ coordinates) and angles of orientation on the field, and the reported values from the IMU-coupled TLG system were recorded. The light intensity on the laser targets, HMT and PMT, was also noted at each numbered location. Furthermore, the robot's XY position was recorded every one second by both systems to generate its horizontal trajectory on the designed path. To validate the system's outdoor capability in daylight and ensure the stringency of the statistical analysis, the system demonstration was repeated five to ten times at each numbered location under various light intensities on the field ranging from 45,000 lux to 85,000 lux during the day time.

The robot's actual position and orientation ($\hat{R}_l$) at the l^{th} location is defined as:

$$\hat{R}_l = (\hat{X}_l, \hat{Y}_l, \hat{Z}_l, \hat{\alpha}_l, \hat{\theta}_l, \hat{\phi}_l) \tag{6}$$

The system's reported (R_{li}) position and orientation of i^{th} epoch at the l^{th} location is defined as:

$$R_{li} = (X_{li}, Y_{li}, Z_{li}, \alpha_{li}, \theta_{li}, \phi_{li}) \tag{7}$$

TABLE 2. The actual position and orientation of the skid-steering robot physically verified at each numbered location on the field.

Location (l)	Distance from the laser base station (cm)	Average light intensity on HMT and PMT (lux)	$\hat{X}_l$ (cm)	$\hat{Y}_l$ (cm)	$\hat{Z}_l$ (cm)	$\hat{\alpha}_l$ (°)	$\hat{\theta}_l$ (°)	$\hat{\phi}_l$ (°)
1	1,000	9,266	-1,000	0	0	0	-2	-1
2	1,415	9,416	-1,000	1,000	-1	0	-2	-1
3	2,237	16,462	-1,000	2,000	-2	90	0	-3
4	2,023	9,108	-300	2,000	-1	180	2	2
5	1,045	8,847	-300	1,000	0	180	1	1
6	300	16,563	-300	0	0	90	0	1
7	300	8,918	300	0	1	0	-1	-1
8	2,023	16,752	300	2,000	0	90	-1	0
9	2,237	9,374	1,000	2,000	0	180	0	-2
10	1,000	5,874	1,000	0	2	-90	1	-1

The system's average reported position and orientation ($\bar{R}_l$) and the standard deviation (σ_l) at the l^{th} location are computed as follows:

$$\bar{R}_l = \frac{1}{N_l}\sum_{i=1}^{N_l} R_{li} \tag{8}$$

where N_l is the total number of epochs at the l^{th} location.

$$\sigma_l = \sqrt{\frac{1}{N_l - 1}\sum_{i=1}^{N_l}(R_{li} - \bar{R}_l)^2} \tag{9}$$

The system's position and orientation accuracy (A_l) at each numbered location are reported as the absolute difference between the robot's actual position and orientation ($\hat{R}_l$) and the system's average reported values ($\bar{R}_l$), which can be expressed as:

$$A_l = \left|\bar{R}_l - \hat{R}_l\right| \tag{10}$$

By averaging A_l from all numbered location, the overall system's position and orientation accuracy (A_{OA}) can be determined as follows:

$$A_{OA} = \frac{1}{M}\sum_{l=1}^{M} A_l \tag{11}$$

where M is the total number of the measured locations.

The system's position and orientation precision at each numbered location is reported as the standard deviation (σ_l) of the measurements at that numbered location. The system's overall position and orientation precision (P_{OA}) are quantified as the combined standard deviation of the system's reported position and orientation at all numbered locations. Since the acquired measurement at each location is independent of one another, the standard deviations were combined using a weighted sum of variance. Hence, the system's P_{OA} is expressed as:

$$P_{OA} = \sqrt{\frac{\sum_{l=1}^{M}(N_l - 1)\sigma_l^2}{\sum_{l=1}^{M}(N_l - 1)}} \tag{12}$$

XI. RESULT AND DISCUSSION

For the determination of the system's accuracy, the actual position and orientation of the robot and the light intensity on the HMT and the PMT at each numbered location were physically verified and reported, as summarized in Table 2. After multiple measurements at each numbered location, the robot's average XYZ coordinates, headings, and attitudes with the computed local accuracy reported by the IMU-coupled TLG system are shown in Table 3. The overall accuracies for X, Y, Z, α, θ, and ϕ reported by the IMU-coupled TLG system are within 0.92 cm, 1.37 cm, 0.59 cm, 0.90°, 0.78°, and 0.76°, respectively. The local maximum errors and standard deviations at each numbered location reported by the IMU-coupled TLG system are presented in Table 4. The overall precisions for X, Y, Z, α, θ, and ϕ reported by the IMU-coupled TLG system are within 0.75 cm, 0.69 cm, 0.67 cm, 0.96°, 0.71°, and 0.59°, respectively. The overall maximum errors for X, Y, Z, α, θ, and ϕ reported by the IMU-coupled TLG system are 3.00 cm, 4.00 cm, 2.00 cm, 3.00°, 3.00°, and 2.20°, respectively. Overall maximum error, accuracy, and precision of the robot's position and orientation reported by the IMU-coupled TLG system are summarized in Table 5. Moreover, a multipass, horizontal trajectory of the robot generated by real-time XY position tracking via the IMU-coupled TLG system is depicted in Fig. 10. Hence, the localization and the horizontal path tracking of the IMU-coupled TLG system were found to be highly accurate and precise all along the designed path.

TABLE 3. Average XYZ coordinates, headings, and attitudes of the robot at each numbered location reported by the IMU-coupled TLG system with computed local (A_l) and overall (A_{OA}) accuracy.

Location (l)	X (cm)		Y (cm)		Z (cm)		Heading (°)		Roll (°)		Pitch (°)	
	$\bar{X}_l$	A_l^X	$\bar{Y}_l$	A_l^Y	$\bar{Z}_l$	A_l^Z	$\bar{\alpha}_l$	A_l^α	$\bar{\theta}_l$	A_l^θ	$\bar{\phi}_l$	A_l^ϕ
1	-1,000.67	0.67	0.67	0.67	0.11	0.11	-0.78	0.78	0.33	2.33	0.44	1.44
2	-1,000.78	0.78	1,000.78	0.78	0.00	1.00	0.11	0.11	-0.56	1.44	0.11	1.11
3	-1,001.33	1.33	2,002.00	2.00	-1.22	0.78	89.00	1.00	-0.89	0.89	-3.00	0.00
4	-301.11	1.11	2,002.67	2.67	-0.78	0.22	179.22	0.78	2.44	0.44	2.33	0.33
5	-300.67	0.67	1,001.67	1.67	0.44	0.44	180.00	0.00	0.78	0.22	0.44	0.56
6	-300.33	0.33	0.44	0.44	0.78	0.78	91.33	1.33	0.00	0.00	0.00	1.00
7	300.44	0.44	0.56	0.56	1.56	0.56	1.67	1.67	-0.78	0.22	-0.89	0.11
8	301.11	1.11	2,001.44	1.44	0.33	0.33	88.78	1.22	-0.22	0.78	0.67	0.67
9	1,001.78	1.78	2,001.67	1.67	1.67	1.67	178.89	1.11	1.33	1.33	-1.44	0.56
10	1,001.00	1.00	1.78	1.78	2.00	0.00	-89.00	1.00	1.11	0.11	0.78	1.78
Overall Accuracy	$A_{OA}^X = 0.92$ cm		$A_{OA}^Y = 1.37$ cm		$A_{OA}^Z = 0.59$ cm		$A_{OA}^\alpha = 0.90°$		$A_{OA}^\theta = 0.78°$		$A_{OA}^\phi = 0.76°$	

TABLE 4. Maximum errors and standard deviations of XYZ coordinates, headings, and attitudes of the robot reported by the IMU-coupled TLG system with computed overall precision (P_{OA}).

Location (l)	X (cm)		Y (cm)		Z (cm)		Heading (°)		Roll (°)		Pitch (°)	
	Absolute Maximum Error	σ_l^X	Absolute Maximum Error	σ_l^Y	Absolute Maximum Error	σ_l^Z	Absolute Maximum Error r	σ_l^α	Absolute Maximum Error	σ_l^θ	Absolute Maximum Error	σ_l^ϕ
1	2.00	0.87	2.00	0.71	1.00	0.60	3.00	1.39	2.00	0.87	2.20	0.88
2	3.00	1.09	2.00	0.67	2.00	0.71	1.00	0.60	2.00	0.73	2.00	0.60
3	3.00	1.00	4.00	1.12	1.00	0.44	2.00	1.00	2.00	0.78	1.00	0.50
4	2.00	0.60	4.00	0.87	1.00	0.44	3.00	1.20	1.00	0.53	1.00	0.50
5	2.00	0.71	2.00	0.50	1.00	0.53	0.00	0.00	1.00	0.44	1.00	0.53
6	1.00	0.50	1.00	0.53	2.00	0.83	3.00	1.12	0.00	0.00	1.00	0.00
7	1.00	0.53	1.00	0.53	1.00	0.73	3.00	1.00	1.00	0.67	1.00	0.33
8	2.00	0.78	2.00	0.53	2.00	1.12	3.00	0.83	3.00	1.09	2.00	0.71
9	3.00	0.67	3.00	0.71	2.00	0.50	2.00	0.93	2.00	0.50	2.00	0.73
10	2.00	0.50	2.00	0.44	1.00	0.50	2.00	0.87	2.00	0.93	2.00	0.67
Overall Maximum Error	3.00 cm		4.00 cm		2.00 cm		3.00°		3.00°		2.20°	
Overall Precision	$P_{OA}^X = 0.75$ cm		$P_{OA}^Y = 0.69$ cm		$P_{OA}^Z = 0.67$ cm		$P_{OA}^\alpha = 0.96°$		$P_{OA}^\theta = 0.71°$		$P_{OA}^\phi = 0.59°$	

Since the XYZ and heading measurements by the IMU-coupled TLG system solely rely on the accuracy of HML and PML detection on the HMT and PMT, the laser beam divergence due to its travel distance and sunlight interference could deteriorate the overall accuracy and precision. The local XYZ/heading accuracy and precision at each numbered location were plotted against the mobile unit's distance from the laser base station and the average light intensity on the laser targets. The local XYZ/heading accuracy and precision versus the robot's distance from the laser base at each numbered location are illustrated in Fig. 11(a)-11(d) and Fig. 11(e)-11(h), respectively. Within the given field size, no correlation between the IMU-coupled TLG system's overall accuracy and precision and the mobile unit's

TABLE 5. Summary of overall maximum error, accuracy, and precision of the robot's position and orientation reported by the IMU-coupled TLG system.

IMU-coupled laser-guided system						
Summary	X	Y	Z	Heading	Roll	Pitch
Overall Maximum Error	3.00 cm	4.00 cm	2.00 cm	3.00°	3.00°	2.20°
Overall Accuracy (A_{OA})	0.92 cm	1.37 cm	0.59 cm	0.90°	0.78°	0.76°
Overall Precision (P_{OA})	0.75 cm	0.69 cm	0.67 cm	0.96°	0.71°	0.59°

TABLE 6. Comparison of lateral/heading accuracy and total cost of the IMU-coupled TLG system to the commercially available GNSS-INS systems, NovAtel PwrPak7D-E2 and Trimble BX992.

Overall Accuracy	IMU-coupled TLG	NovAtel PwrPak7D-E2	Trimble BX992
Lateral (A_{OA}^{LAT})	1.68 cm	1.00 cm	5.00 cm
Heading (A_{OA}^{α})	0.90°	0.05°	0.09°
Total Cost (USD)	~$950	~$11,000	~$6,000

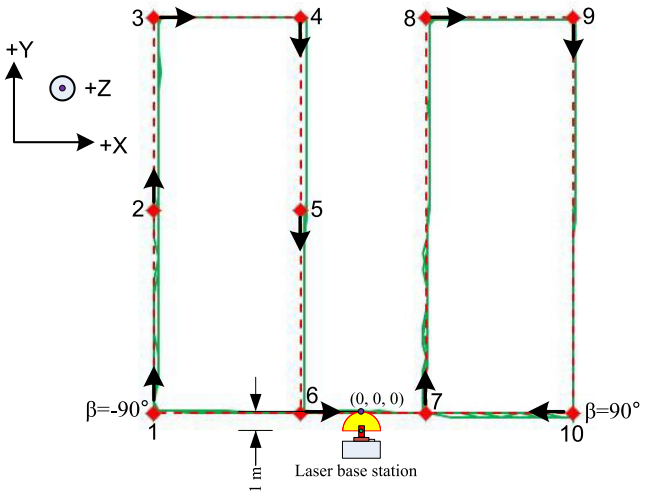

FIGURE 10. Multipass trajectories (solid green line) of the skid-steering robot on the designed path (dotted red line) generated by the real-time position tracking of the IMU-coupled TLG system.

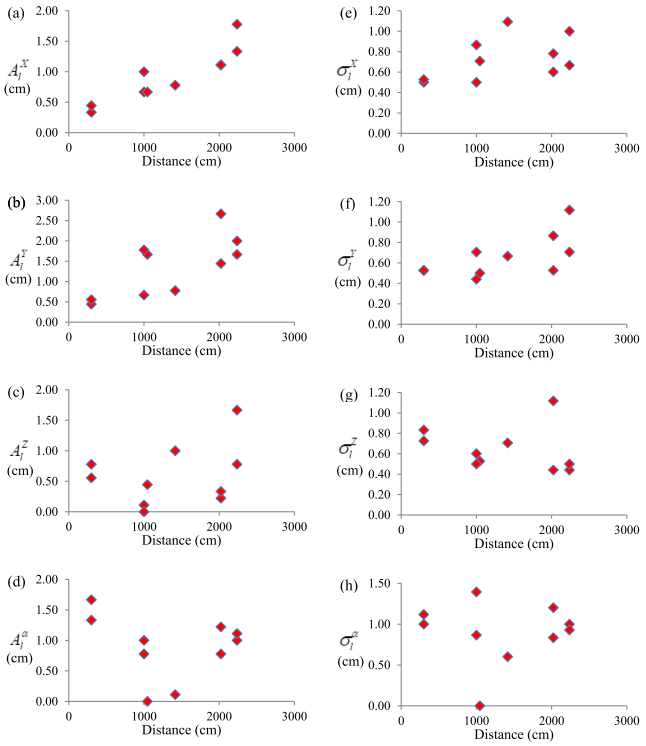

FIGURE 11. The local accuracy (A_l) and precision (σ_l) of the robot's XYZ coordinates and heading reported by the IMU-coupled TLG system at the numbered locations versus the mobile unit's distance from the laser base station.

distance from the laser base station was established. The local XYZ/heading accuracy and precision versus the average light intensity on the laser targets at each numbered location are depicted in Fig. 12(a)-11(d) and Fig. 12(e)-11(h), respectively. If not exceeding 20,000 lux, the varying light intensity on the laser targets during the daytime did not significantly affect the system's overall accuracy and precision.

The overall localization performance and the total cost of the IMU-coupled TLG system are compared to those of the commercially available GNSS-INS systems, namely NovAtel PwrPak7D-E2 and Trimble BX992. The performance comparison criteria are lateral accuracy (A_{OA}^{LAT}) and heading accuracy (A_{OA}^{α}). The lateral accuracy of the IMU-coupled TLG system is computed from the overall XYZ accuracies (A_{OA}^{X} and A_{OA}^{Y} as shown in Table 5) using the equations as follows:

$$A_{OA}^{LAT} = \sqrt{(A_{OA}^{X})^2 + (A_{OA}^{Y})^2} \tag{13}$$

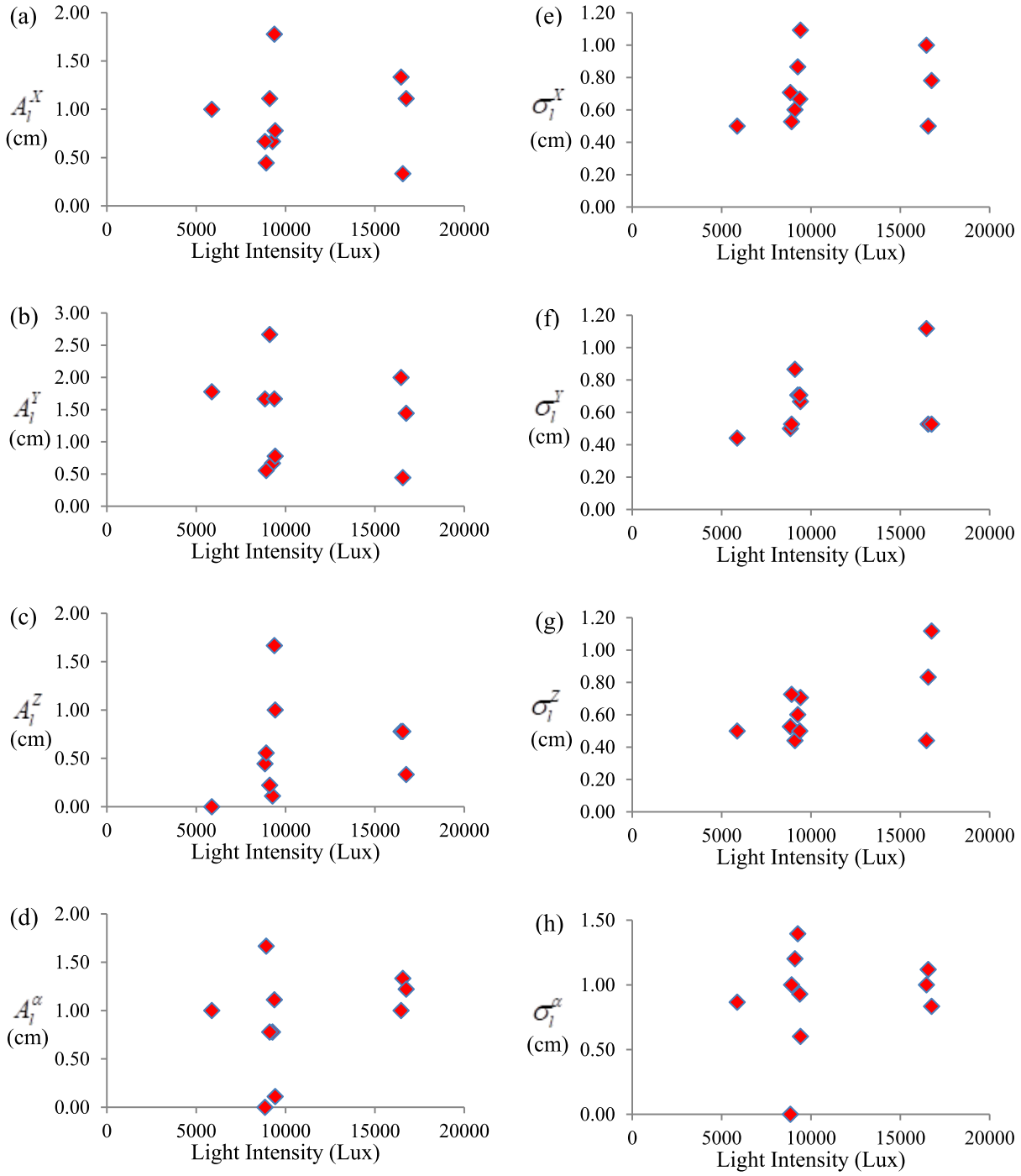

FIGURE 12. The local accuracy (A_l) and precision (σ_l) of the robot's XYZ coordinates and heading reported by the IMU-coupled TLG system at the numbered locations versus the average light intensity on the HMT and PMT.

The comparison of the IMU-coupled TLG system with the NovAtel PwrPak7D-E2 and Trimble BX992 is summarized in Table 6. The lateral and heading accuracies of NovAtel PwrPak7D-E2 and Trimble BX992 are based on the best performance claimed by their system specifications. The lateral accuracies of the IMU-coupled TLG system, NovAtel PwrPak7D-E2, and Trimble BX992 are 1.68 cm, 1.00 cm, 5.00 cm, respectively. The heading accuracies of the IMU-coupled TLG system, NovAtel PwrPak7D-E2, and Trimble BX992 are 0.90°, 0.05°, and 0.09°, respectively. This shows that the localization performance of the IMU-coupled TLG system is comparable to those of the commercially available GNSS-INS systems. Furthermore, while the GNSS-INS systems are limited only for an open, outdoor environment under optimal open-sky conditions, the IMU-coupled TLG system can operate in both indoor and

outdoor settings with the only outdoor limitations of rainy weather and maximum light intensity of 20,000 lux.

The total cost of the IMU-coupled TLG system is approximately $950 in USD, while those of NovAtel PwrPak7D-E2 and Trimble BX992 are approximately $11,000 in USD and $6,000 in USD, respectively. The costs of the NovAtel PwrPak7D-E2 and Trimble BX992 are based on the actual online prices in February 2021, which may vary depending on the location. Also, there is an additional yearly cost for GNSS correction services, i.e., for this instance, TerraStar for NovAtel GNSS receivers and Trimble-RTX for Trimble receivers. The prices and availability of the GNSS correction services may vary depending on the geographical location. If the GNSS correction service is unavailable in the desired area of operation, a separate GNSS base is required, which may add up to $12,000 in USD into the total cost of the GNSS-INS system. This can be concluded that the total cost of the IMU-coupled TLG system is at least five times less expensive compared to the commercially available GNSS-INS systems in the current market.

XII. CONCLUSION

After repeated robot's position and orientation measurements on a 20 × 21 m flat, open field, the IMU-coupled TLG system with a total cost of only $950 in USD reported the lateral and heading accuracy of 1.68 cm and 0.90°, respectively. The lateral and heading accuracy performances are comparable to those of commercially available GNSS-INS localization systems. The multipass horizontal path tracking also confirmed the high accuracy and precision of the IMU-coupled TLG system. Furthermore, the IMU-coupled TLG system reliably performed with various light intensities on the laser targets under 20,000 lux without any noticeable deterioration in localization accuracy and precision. Hence, this novel IMU-coupled TLG system presents a new promising solution as a low-cost, high-accuracy alternative for automatic machinery in the agricultural industry.

REFERENCES

[1] F. Aghili and A. Salerno, "Attitude determination and localization of mobile robots using two RTK GPSs and IMU," in *Proc. IEEE/RSJ Int. Conf. Intell. Robots Syst.*, Oct. 2009, pp. 2045–2052, doi: 10.1109/IROS.2009.5354770.

[2] P. Mayer, M. Magno, A. Berger, and L. Benini, "RTK-LoRa: High-precision, long-range, and energy-efficient localization for mobile IoT devices," *IEEE Trans. Instrum. Meas.*, vol. 70, Oct. 2021, Art. no. 3000611, doi: 10.1109/TIM.2020.3042296.

[3] M. Pini, G. Marucco, G. Falco, M. Nicola, and W. De Wilde, "Experimental testbed and methodology for the assessment of RTK GNSS receivers used in precision agriculture," *IEEE Access*, vol. 8, pp. 14690–14703, Jan. 2020, doi: 10.1109/ACCESS.2020.2965741.

[4] D. S. M. Valente, A. Momin, T. Grift, and A. Hansen, "Accuracy and precision evaluation of two low-cost RTK global navigation satellite systems," *Comput. Electron. Agricult.*, vol. 168, Jan. 2020, Art. no. 105142.

[5] X. Yin, J. Du, D. Geng, and C. Jin, "Development of an automatically guided rice transplanter using RTK-GNSS and IMU," *IFAC-PapersOnLine*, vol. 51, no. 17, pp. 374–378, Sep. 2018.

[6] D. Nemec, V. Šimák, A. Janota, M. Hruboš, and E. Bubeníková, "Precise localization of the mobile wheeled robot using sensor fusion of odometry, visual artificial landmarks and inertial sensors," *Robot. Auto. Syst.*, vol. 112, pp. 168–177, Feb. 2019.

[7] T. Le, J. G. O. Gjevestad, and P. J. From, "Online 3D mapping and localization system for agricultural robots," *IFAC-PapersOnLine*, vol. 52, no. 30, pp. 167–172, 2019.

[8] D. Shi, H. Mi, E. G. Collins, and J. Wu, "An indoor low-cost and high-accuracy localization approach for AGVs," *IEEE Access*, vol. 8, pp. 50085–50090, Mar. 2020, doi: 10.1109/ACCESS.2020.2980364.

[9] R. P. Guan, B. Ristic, L. Wang, and R. Evans, "Monte Carlo localisation of a mobile robot using a Doppler–Azimuth radar," *Automatica*, vol. 97, pp. 161–166, Nov. 2018.

[10] N. Shalal, T. Low, C. McCarthy, and N. Hancock, "Orchard mapping and mobile robot localisation using on-board camera and laser scanner data fusion—Part A: Tree detection," *Comput. Electron. Agricult.*, vol. 119, pp. 254–266, Nov. 2015.

[11] H. Fang, C. Wang, M. Yang, and R. Yang, "Ground-texture-based localization for intelligent vehicles," *IEEE Trans. Intell. Transp. Syst.*, vol. 10, no. 3, pp. 463–468, Sep. 2009, doi: 10.1109/TITS.2009.2026445.

[12] J.-H. Shim and Y.-I. Cho, "A mobile robot localization using external surveillance cameras at indoor," *Procedia Comput. Sci.*, vol. 56, no. 1, pp. 502–507, Jul. 2015.

[13] J. Xue, L. Zhang, and T. E. Grift, "Variable field-of-view machine vision based row guidance of an agricultural robot," *Comput. Electron. Agricult.*, vol. 84, pp. 85–91, Jun. 2012.

[14] P. Hoppenot and E. Colle, "Real-time mobile robot localisation with poor ultrasonic data," *IFAC Proc. Volumes*, vol. 30, no. 7, pp. 131–136, Jun. 1997.

[15] S. J. LeVoir, P. A. Farley, T. Sun, and C. Xu, "High-accuracy adaptive low-cost location sensing subsystems for autonomous rover in precision agriculture," *IEEE Open J. Ind. Appl.*, vol. 1, pp. 74–94, Aug. 2020, doi: 10.1109/OJIA.2020.3015253.

[16] A. Canedo-Rodríguez, V. Álvarez-Santos, C. V. Regueiro, R. Iglesias, S. Barro, and J. Presedo, "Particle filter robot localisation through robust fusion of laser, WiFi, compass, and a network of external cameras," *Inf. Fusion*, vol. 27, pp. 170–188, Jan. 2016.

[17] A. P. Moreira, P. Costa, and J. Lima, "New approach for beacons based mobile robot localization using Kalman filters," *Procedia Manuf.*, vol. 51, pp. 512–519, Nov. 2020.

[18] Z. Niu, X. Zhao, J. Sun, L. Tao, and B. Zhu, "A continuous positioning algorithm based on RTK and VI-SLAM with smartphones," *IEEE Access*, vol. 8, pp. 185638–185650, 2020, doi: 10.1109/ACCESS.2020.3028119.

[19] L. Wei, C. Cappelle, and Y. Ruichek, "Camera/laser/GPS fusion method for vehicle positioning under extended NIS-based sensor validation," *IEEE Trans. Instrum. Meas.*, vol. 62, no. 11, pp. 3110–3122, Nov. 2013, doi: 10.1109/TIM.2013.2265476.

[20] P. Gui, L. Tang, and S. Mukhopadhyay, "MEMS based IMU for tilting measurement: Comparison of complementary and Kalman filter based data fusion," in *Proc. IEEE 10th Conf. Ind. Electron. Appl. (ICIEA)*, Jun. 2015, pp. 2004–2009, doi: 10.1109/ICIEA.2015.7334442.

[21] G. He, X. Yuan, Y. Zhuang, and H. Hu, "An integrated GNSS/LiDAR-SLAM pose estimation framework for large-scale map building in partially GNSS-denied environments," *IEEE Trans. Instrum. Meas.*, vol. 70, Sep. 2021, Art. no. 7500709, doi: 10.1109/TIM.2020.3024405.

[22] H. Lan, M. Elsheikh, W. Abdelfatah, A. Wahdan, and N. El-Sheimy, "Integrated RTK/INS navigation for precision agriculture," in *Proc. 32nd Int. Tech. Meeting Satell. Division Inst. Navigat. (ION GNSS)*, Oct. 2019, pp. 4076–4086.

[23] P. Zhang, Y. Zhao, H. Lin, J. Zou, X. Wang, and F. Yang, "A novel GNSS attitude determination method based on primary baseline switching for a multi-antenna platform," *Remote Sens.*, vol. 12, no. 5, p. 747, Feb. 2020.

[24] B. Schnaufer, G. McGraw, H. Phan, and A. Joseph, "GNSS-based dual-antenna heading augmentation for attitude and heading reference systems," in *Proc. 29th Int. Tech. Meeting Satell. Division Inst. Navigat. (ION GNSS)*, Nov. 2016, pp. 3669–3691.

[25] P. Fan, W. Li, X. Cui, and M. Lu, "Precise and robust RTK-GNSS positioning in urban environments with dual-antenna configuration," *Sensors*, vol. 19, no. 16, p. 3586, Aug. 2019.

[26] Z. Zhe, W. Jian-bin, S. Bo, and T. Guo-feng, "Adaptive complementary filtering algorithm for IMU based on MEMS," in *Proc. Chin. Control Decis. Conf. (CCDC)*, Aug. 2020, pp. 5409–5416, doi: 10.1109/CCDC49329.2020.9164809.

[27] T. Ngo, P. Nguyen, S. Huynh, S. Le, and T. Nguyen, "Filter design for low-cost sensor in quadcopter," in *Proc. Int. Conf. Syst. Sci. Eng.*, Sep. 2017, no. 3, pp. 488–493, doi: 10.1109/ICSSE.2017.8030922.

SUPOD KAEWKORN received the B.Eng. degree in electrical engineering from Kasembundit University, Bangkok, Thailand, in 1998, and the M.Eng. degree in computer engineering from the King Mongkut's University of Technology Ladkrabang, Bangkok, in 2003. He is currently pursuing the Ph.D. degree in mechatronics with the School of Engineering and Technology, Asian Institute of Technology, Thailand. He joined the Mechatronics Engineering Technology Division, Department of Mechanical Engineering Technology, College of Industrial Technology, King Mongkut's University of Technology North Bangkok, in 2010, where he is currently an Assistant Professor. His research interests include automatic control systems, computer control, microcontroller, deep learning, and embedded systems.

MONGKOL EKPANYAPONG received the B.Eng. degree in computer engineering from Chulalongkorn Univerisity, Bangkok, Thailand, in 1997, the M.Eng. degree in computer science from the Asian Institute of Technology, Thailand, in 2000, and the M.Sc. and Ph.D. degrees in electrical and computer engineering from the Georgia Institute of Technology, Atlanta, GA, USA, in 2003 and 2006, respectively. From 1997 to 1998, he was a System Engineer with United Communication Network, Thailand. From 2006 to 2009, he was a Senior Computer Architect with Core 2 Architecture Design Team, Intel Corporation, USA. He joined the School of Engineering and Technology, Asian Institute of Technology, in 2009, where he is currently an Associate Professor. His research interests include VLSI design, physical design automation, microarchitecture, compiler, and embedded systems.

UKRIT THAMMA received the B.Sc., M.Eng., and Ph.D. degrees in materials science and engineering from Lehigh University, Bethlehem, PA, USA, in 2011, 2012, and 2017, respectively. From 2011 to 2017, he was a Research Assistant with the International Materials Institute for New Functionality, Glass, Lehigh University. He joined the Department of Mechanical Engineering Technology, College of Industrial Technology, King Mongkut's University of Technology North Bangkok, Bangkok, Thailand, in 2017, where he is currently a Lecturer in materials science and engineering courses. His research interests include bioactive glasses for hard tissue engineering, metallurgy and manufacturing processes for medical applications, and automation for agricultural applications.